



CHORUS

This is the accepted manuscript made available via CHORUS. The article has been published as:

Intrinsic point defects and intergrowths in layered bismuth triiodide

Sung Beom Cho, Jaume Gazquez, Xing Huang, Yoon Myung, Parag Banerjee, and Rohan Mishra

Phys. Rev. Materials **2**, 064602 — Published 7 June 2018

DOI: [10.1103/PhysRevMaterials.2.064602](https://doi.org/10.1103/PhysRevMaterials.2.064602)

Intrinsic point defects and intergrowths in layered bismuth triiodide

Sung Beom Cho,^{*†} Jaume Gazquez,[§] Xing Huang,^{†,⊥} Yoon Myung,^{†,||} Parag Banerjee,^{†,‡} and Rohan Mishra^{*†,‡}

[†]Department of Mechanical Engineering and Materials Science, Washington University in St. Louis, St. Louis, Missouri 63130, United States

[§]Institut de Ciència de Materials de Barcelona, Barcelona 08193, Spain

[‡]Institute of Materials Science and Engineering, Washington University in St. Louis, St. Louis, Missouri 63130, United States

ABSTRACT

Defect-tolerant semiconductors have the ability to retain the electronic properties of their pristine form even in the presence of defects. Currently, the presence of antibonding states at the valence band edges induced by a lone pair of $6s^2$ or $5s^2$ electrons is used as a descriptor to predict defect-tolerant semiconductors. Based on this descriptor, bismuth triiodide (BiI_3) has been proposed as a defect-tolerant semiconductor with promise for photovoltaic applications. However, clear demonstration of the defect tolerance of BiI_3 including a comprehensive study of the type of defects and their effect on the electronic structure has not been reported so far. Here, we present an atomic-scale landscape of point defects and intergrowths in BiI_3 using a combination of density-functional-theory (DFT) calculations and aberration-corrected scanning transmission electron microscope (STEM) imaging. We show that BiI_3 is not a defect-tolerant semiconductor as intrinsic point defects have low formation energy and show transition levels that are deep within the band gap and can act as non-radiative recombination centers. We show that Bi-rich growth conditions lead to higher carrier concentration over I-rich conditions. We also show the presence of intergrowths that are made up of a bilayer of bismuth atoms sandwiched within BiI_3 sheets with a missing layer of iodine atoms. These intergrowths result in metallic behavior within the semiconducting matrix of BiI_3 . We propose that atomic-scale control of the intergrowths can be beneficial to avoid carrier trapping and to enhance photon absorbance. Overall, this work highlights the need to go beyond heuristic descriptors based on band edge characteristics to predict defect-tolerant semiconductors.

INTRODUCTION

Lead-halide perovskites have rapidly emerged as a new class of affordable, high-performance semiconductors with applications in high-efficiency photovoltaics and optoelectronics [1,2]. The fast solution-based deposition techniques used to grow these materials combined with the instability and degradation issues that plague them result in a large concentration of defects [2,3]; however, the electronic properties of lead-halide perovskites are found to be largely unaltered [4-6]. This ability of a semiconductor to retain its electronic structure and properties, despite the presence of defects has been termed as defect tolerance [7-9]. The defect tolerance of lead-halide perovskites has been attributed to the presence of occupied $6s^2$ lone-pair of electrons on the Pb^{2+} cation [10,11]. The lone-pair electrons result in a large dielectric constant that can efficiently screen charged defects [12]. They also lead to antibonding states at the valence band edge, which leads to defect states that are either shallow or within the band edges [6,7,10,13].

The stability and degradation issues of lead-halide perovskites [14-17], combined with the toxic nature of lead have resulted in an active search for stable, defect-tolerant compounds based on environmentally benign heavy elements that can substitute lead halides without compromising the performance of the semiconductors [18,19]. Amongst the various proposed alternatives, bismuth halides are particularly promising because Bi^{3+} is isoelectronic with Pb^{2+} having occupied $6s^2$ lone-pair electrons, and is environmentally benign [20-29]. One of the simplest possible bismuth halides is bismuth triiodide (BiI_3), which is a layered semiconductor with a moderate bandgap of 1.8 eV [30]. Traditionally, it has been studied as a material for detecting X-rays and γ -rays due to its high electron-hole pair generation efficiency [31], high density (5.8 g/cm^3) and the large atomic number of Bi ($Z_{Bi} = 83$) and I ($Z_I=53$) [32-36]. Recently, BiI_3 has also been proposed as a defect-tolerant semiconductor with special promise for

photovoltaic applications due to the presence of antibonding states at the valence band edge and a large absorption coefficient ($>10^5 \text{ cm}^{-1}$) in the visible region of the solar spectrum [10,37]. Till date, however, the defect tolerance of BiI_3 remains unknown due to the lack of understanding of common defects, including point defects and extended defects that form in this material, and their effect on the electronic structure.

In this study, we present a comprehensive picture of the atomic-scale defect landscape of BiI_3 using a combination of density functional theory (DFT) calculations and aberration-corrected scanning transmission electron microscopy (STEM). By calculating all possible intrinsic point defects, we have identified the favorable defects under various growth conditions and their effect on carrier concentration and conductivity. We find bismuth interstitials, bismuth antisites and iodine vacancies are favorable to form under Bi-rich (I-poor) conditions, while bismuth vacancies and iodine antisites are dominant under I-rich conditions. In contrast to the claimed defect tolerance of BiI_3 , we find that all the dominant point defects lead to deep-level traps and are expected to play a role as recombination centers. Furthermore, STEM analysis shows the presence of an extensive network of bilayer Bi intergrowths sandwiched within BiI_3 sheets with a missing layer of iodine atoms that span 3–8 nm in the solution-phase deposited films. The presence of these intergrowths provides two-dimensional metallic conductive pathways that might promote carrier separation and reduce recombination. The atomic-scale control of these stacking faults is expected to enhance the photovoltaic properties of BiI_3 .

RESULTS AND DISCUSSION

Bulk BiI_3

BiI₃ particles were synthesized using a solution process described in the Methods section. We find the BiI₃ particles have a hexagonal morphology with an average particle size of 5 μm, as shown in the SEM image in Fig. 1a. Based on X-ray diffraction analysis (see Supplemental Materials [67]), we find BiI₃ has a rhombohedral crystal structure with $R\bar{3}$ space group, as shown in Fig. 1b, in agreement with the literature [38]. BiI₃ consists of I-Bi-I trilayers that are loosely held together with van der Waals (vdW) forces. Within the Bi layers, the atoms occupy 2/3rd of the available sites and are octahedrally coordinated by the iodine atoms. Each BiI₆ octahedron is connected to three neighboring octahedra through shared edges. We have calculated the electronic structure of BiI₃ using the Perdew-Burke-Ernzerhof (PBE) exchange-correlation functional [39] including spin-orbit coupling effects. We find the DFT-optimized lattice parameters to be 7.83 Å for in plane and 22.55 Å for normal-plane, which are within 4 % and 8.8 % of the experimental values, respectively. The overestimation for normal-plane is due to the choice of exchange-correlation functional, which lacks vdW forces (see Supplemental Materials [67]). Though the obtained value is consistent with a previous study [40], we fixed the lattice constants to their experimental values to address this discrepancy. We find the valence band is predominantly composed of 5*p* states of I with a small contribution from the 6*s* states of Bi, while the conduction band consists of 5*p* states of Bi and I, as shown in Fig. 1d, which also includes the calculated band structure. We obtain an indirect band gap of 1.61 eV, which agrees well with the experimentally measured value of 1.60 eV, as shown in the UV-vis plot in Fig. 1e. The direct theoretical band gap is slightly larger with a value of 1.69 eV, whereas the experimentally measured direct band gap is 1.80 eV. Though the calculated bandgap shows good agreement with the experimental measurements — in line with previous theoretical reports [27,30,37] — this is likely to be serendipitous as our DFT calculations do not capture the strong

excitonic effects observed experimentally in BiI₃. We have carried out the defect analysis using the PBE functional with SOC effects while keep the lattice constants fixed to their experimental values and by only optimizing the atom coordinates.

Intrinsic point defects in BiI₃

To identify the dominant point defects in BiI₃, their concentration and their effect on the electronic properties, we have calculated the formation energy of all possible intrinsic point defects under various chemical and electronic potential (Fermi level). The considered defects include Bi and I vacancies (V_{Bi} , V_{I}), interstitial sites within the I layer corresponding to Wyckoff position 18f ($\text{Bi}_{18\text{f}}$, $\text{I}_{18\text{f}}$) and within the Bi layer at Wyckoff position 6c ($\text{Bi}_{6\text{c}}$, $\text{I}_{6\text{c}}$), and substitutional defects or antisites (Bi_{I} , I_{Bi}). The atomic configurations of these point defects are shown in Fig. 2a. The formation energy of each defect, $\Delta H_f(D^q)$, where q is the charge state of the defect D , is calculated under three representative preparation conditions: Bi-rich (I-poor), I-rich (Bi-poor) and intermediate conditions (shown in Supplemental Materials [67]), which constrain the chemical potential of each element, μ_i . As the defects can have different charge states by exchanging electrons with the Fermi level E_{F} , we have calculated their stability by varying E_{F} across the entire band gap. More details about the calculation of formation energies are provided in the Methods section.

The calculated formation energy of all the intrinsic point defects as a function of E_{F} under the two extreme preparation conditions is shown in Fig. 2b. In these plots, the slope of the lines denotes the charge-state of the defects with a positive (negative) slope denoting a tendency to donate (accept) electrons to (from) the bulk. Under Bi-rich conditions, Bi_{I} , $\text{Bi}_{18\text{f}}$, $\text{Bi}_{6\text{c}}$ and V_{I} have formation energy lower than 2 eV for E_{F} spanning the entire band gap and are expected to exist

in finite concentrations. On increasing the Fermi level from the valence band, each of these point defects shows a transition from a positive to a neutral charge state near the midgap region. Thus, they have a large ionization energy and are expected to act as “deep” donors without any significant contribution to *n*-type conductivity.

The deep level of the defects indicates that BiI₃ is not a defect-tolerant semiconductor. In defect-tolerant semiconductors, the formation of deep-level defects is suppressed and shallow defects are promoted, which has been hypothesized to be due to the presence of antibonding states at the valence band edge and bonding states at the conduction band [9,41,42]. However, we find the conduction band edge in BiI₃ is dominated by antibonding states as shown in the Crystal Orbital Hamiltonian Population (COHP) analysis in Fig. 2c. This implies that BiI₃ does not fully satisfy the conditions for defect tolerance. Contrary to the hypothesis of defect tolerance in BiI₃ simply due to the presence of antibonding states at valence band arising from Bi-6s² lone pair electrons [10,37], every intrinsic defect shows transition levels deep within the band gap, as shown in Fig. 2d. Such deep-level defects can be expected to act as electron-hole recombination centers and as sites that can trap the carriers. Furthermore, the large static dielectric constant of BiI₃ ($\epsilon_{\parallel}=54$, $\epsilon_{\perp}=8.6$) [11] can be expected to screen the charged point defects and reduce their charge-capture cross-section; however, the low formation energy of the point defects, and consequently their large concentration, is likely to counter the effects of a reduced charge-capture cross-section and result in degradation of the carrier diffusion length and mobility. Our observation of the deep level of the point defects in BiI₃ that can act as trap centers agrees well with the formation energies and short carrier-lifetime reported recently [24,43].

Similarly, we observe deep transition levels for defects under I-rich preparation conditions. All native defects, except interstitial and substitutional Bi defects, can have considerably low

formation energy depending on E_F . Thus, the overall defect concentration is expected to be much higher under I-rich conditions than under Bi-rich conditions. This implies that from a synthesis perspective, it is beneficial to grow BiI_3 under Bi-rich conditions to yield lower defect concentrations. We find V_{Bi} , I_{18f} , I_{6c} , and I_{Bi} act as deep acceptors and trapping sites. These deep-level defects can also hinder intentional doping by impurities. For instance, the deep acceptors can capture electrons donated by n -type dopants and prevent successful doping. Another important consideration for the I-rich preparation condition is the role of V_{I} , which has low formation energy closer to the valence band. V_{I} is a deep donor and can, therefore, compensate p -type carriers. It is therefore expected to play an important role in determining the equilibrium E_F of BiI_3 , as discussed below.

Fig. 2e shows the calculated equilibrium Fermi level as a function of temperature (T) for different growth conditions and carrier concentration. Under I-rich conditions, the equilibrium Fermi level is located at the middle of the band gap at 0.85 eV above the valence band maximum (VBM) and is nearly independent of T . Similarly, under Bi-rich conditions, the Fermi level is located between 1.1-1.2 eV for T up to 503 K, which is the sublimation temperature of BiI_3 [44]. This weak temperature-dependency is due to the co-existence of deep donors and acceptors. Both electrons and holes are, respectively, trapped by either deep acceptors or donors, which pin the Fermi level. We expect that external doping is unlikely to result in any increase in carrier concentration until the deep-level defects are compensated. Thus, we predict that in order to successfully use external doping to increase conductivity, the concentration of deep-level defects has to be minimized.

BiI_3 microstructure

To unambiguously resolve the local disorder in BiI₃ films we have used aberration-corrected STEM. High-angle annular dark-field (HAADF) STEM imaging provides directly interpretable and chemically sensitive images at the atomic level [45,46]. Fig. 3a shows a STEM image of a region of the BiI₃ film free from any apparent defects. The HAADF signal scales approximately with the square of the atomic number Z [45,46]. Thus, Bi atoms appear brighter in the image than the lighter I atoms. Because Bi occupies only 2/3rd of the available lattice sites, the periodically vacant site in the central Bi layer can be clearly observed along the [010] orientation. On the other hand, iodine planes show no vacant sites. As expected, the I-Bi-I trilayers are 3.26 Å apart and are held together by weak van der Waals forces.

A detailed inspection of the Z -contrast images of the film shows the presence of some of the point defects described above. The inset in Fig. 3a shows a magnified image of the BiI₃ matrix in which Bi_I and V_I can be seen. The former shows up as a brighter I-atomic column while the latter as a dimmer one (See Supplemental Materials [67]).

Occasionally, the film shows a patched structure stemming from the presence of short Bi-Bi bilayers separated from BiI₃ by a monolayer of iodine atoms, as shown Fig. 3b. These are substitutional Bi_I atoms that preferentially occupy one of the two I layers and form a chain of Bi–Bi–I. The low formation energy of Bi_I substitutional defects under Bi-rich conditions (Fig. 2b) makes formation of such defects possible. The Bi–Bi bilayer is then observed to split off from the I layer and span a length of 3-8 nm. These bilayer defects can be ruled out as screw dislocations such as those formed during helicoidal growth [47]. [This is because in a screw dislocation the dislocation line and the Burgers vector are parallel, so the dislocation may slip on any plane on which it lies. Such a case can be ruled out from the STEM images, as the contrast observed in the images cannot be obtained by superimposing any integer multiple of the BiI₃ unit](#)

cell. Therefore, we conclude that the observed defects are non-stoichiometric planar intergrowths made up of the dominant point defects.

To understand the three-dimensional atomic configuration of these intergrowths, we have constructed the atomic structure considering the defect energetics and STEM images. According to the STEM images, we find $1/3^{\text{rd}}$ of the vacant sites in the Bi intralayer are occupied by Bi_{6c} interstitials. Another feature of the Bi-Bi bilayer is that all the lattice sites in the I intralayer are substituted with Bi atoms. Thus, we constructed Bi-Bi bilayers by adding Bi_{6c} to all the vacant sites and by replacing all the I atoms in one of the I-layers by Bi_I antisites, as shown in Fig. 3c. We find this intergrowth defect has a low formation energy of 0.43 eV/(BiI_3 f.u.) under Bi-rich conditions, which is comparable to the energy of non-stoichiometric planar defects in SrTiO_3 (0.57 eV/ SrTiO_3 f.u.).[48] This low formation energy supports the presence of the bilayer Bi intergrowths in the BiI_3 films. To ensure the atomic configuration, we also manipulated the occupancy of Bi_I and Bi_{18f} (See Supplemental Materials [67]); however, we find that if Bi and I coexist in the same intralayer, large atomic distortions occur, making them energetically unfavorable.

To obtain more accurate structural information of the Bi intergrowths, we have performed ionic relaxation by using the DFT-D3 functional, which includes van der Waals (vdW) dispersion forces [49,50] that are known to describe layered structures more accurately [27,40]. We find an out-of-plane lattice constant of 20.62 Å for pristine BiI_3 , which is consistent with the experimental value of 20.72 Å. With the DFT-D3 functional, we also constructed a supercell that consists of two I–Bi–Bi layers as shown in Fig. 3c. We performed STEM image simulations using the optimized atomic structure and compared it with the central region of two Bi intergrowths. The simulated image is shown in Fig. 3d. We find that the constructed model

shows excellent agreement with the layer distances and line-profiles obtained from the experimental STEM image as shown in Fig. 3e. Based on this excellent agreement between the simulated and the experimental Z-contrast images and the low formation energy, we conclude that the optimized model is an accurate representation of the observed Bi intergrowths.

To understand the effect of the Bi intergrowths on the optoelectronic properties of BiI₃, we have calculated the electronic structure of the constructed model. Interestingly, the intergrowth results in a metallic behavior as shown in the layer-resolved density of states (DOS) in Fig. 4a. This is not surprising considering that the atomic configuration of the Bi intergrowth is similar to a monolayer of Bi bulk (See Supplemental Materials [67]). In its bulk form, Bi has a space group of $R\bar{3}c$ and consists of a buckled hexagonal lattice. It is also a semi-metal [51] and displays novel plasmonic behavior [52]. The Bi intergrowths are also expected to show plasmonic behavior as we obtain the plasmon frequency in the isolated Bi-bilayer region to be 2.42 eV/h (513 nm in wavelength). These metallic intergrowths could be used to amplify the intensity of wavelengths in a spectral range corresponding to the plasmonic frequency and improve the efficiency of photovoltaic devices [53,54].

Due to their metallic nature, the formation of the intergrowths within BiI₃ can also be considered as a semiconductor composite embedded with nanoscale two-dimensional metallic regions. Controlled growth and structuring of these metallic Bi-Bi bilayers within BiI₃ by using layer-by-layer growth techniques can lead to an enhancement in the photovoltaic efficiency. For instance, in other photovoltaic semiconductors, such as CdTe and the new class of organic lead halide perovskites, conductive grain boundaries are known to act as pathways for efficient separation of the photogenerated carriers, thereby reducing the recombination rates and enhancing their photovoltaic performance [55-57]. The conductive region creates a built-in field

around itself, and it promotes electron-hole pair separation [58]. Similar photo-induced charge separation is also observed in metal-semiconductor nanocluster composites [59].

We also find that the formation of BiI₃ enhances the absorption as shown in Fig. 4b. The constructed complex cell in Fig. 3d, which is made up of Bi bilayers and pristine BiI₃ with a 2:1 ratio, shows better absorption than pristine BiI₃ in the overall frequency range. This is due to the dielectric contribution of the Bi bilayers [60,61]. The dielectric response of the total system can be described with an Effective Medium Approximation (EMA) [62], and the effective dielectric constant can be expressed by the Maxwell-Garnett equation (MGT) [63]:

$$\epsilon_{\text{eff}} = \epsilon_s \frac{(1 + 2VZ)}{(1 - VZ)}, \text{ where } Z = \frac{(\epsilon_m - \epsilon_s)}{(\epsilon_m + 2\epsilon_s)}. \quad (1)$$

V is volume fraction between metal and semiconductor, and ϵ_s and ϵ_m are the dielectric constants of the semiconductor and metal, respectively. Because the dielectric constant of metallic Bi bilayers is larger than that of BiI₃, the overall dielectric constant of the films is expected to increase. This enhanced dielectric property can screen the effect of defects in BiI₃ and intensify the optical adsorption.

CONCLUSION

We have presented a holistic picture of the common intrinsic defects in BiI₃ and their effect on its electronic properties. Amongst point defects, we find bismuth interstitials, bismuth antisites and iodine vacancies to be the dominant defects under Bi-rich growth conditions, and iodine and bismuth vacancies and iodine antisites to be the dominant defect under I-rich conditions. We show that all the possible defects have deep level character and can act as non-radiative recombination centers and pin the Fermi level. These results are in strong contrast to the

previously proposed defect tolerant nature of BiI₃. It implies that the defect tolerance of a material cannot be determined simply by band-edge characteristics, and a thorough defect analysis is required. Using STEM, we also provide direct evidence, of previously unknown, Bi intergrowths spanning a few nanometers within the semiconducting BiI₃ films. The metallic character of the intergrowths can be expected to enhance the carrier collection and the photovoltaic efficiency of BiI₃.

Taken together, our investigation suggests possible synthesis strategies for defect engineering of BiI₃ for high-performance semiconductors with applications in photovoltaic devices. Since intrinsic point defects degrade photovoltaic properties, the synthesis conditions for BiI₃ should be carefully controlled to minimize their concentration. The metallic nature of the intergrowth as identified in this study can be used to tune the electronic and optical properties of the BiI₃ films. Furthermore, due to the structural similarity of BiI₃ with other Bi-based layered materials, such as Bi₂S₃, Bi₂Se₃, and Bi₂Te₃, the facile formation of stacking faults made up of Bi-bilayers may apply to those materials as well, leading to improved understanding and engineering of Bi-based thermoelectrics. Finally, our work highlights the need for better design-rules to search for defect-tolerant semiconductors as the proposed mechanism of simply using cations with occupied lone-pair electron fails in the case of BiI₃.

METHODS

First-principles DFT calculations

We have performed the first-principles DFT calculations using the Vienna Ab-initio Simulation Package^{37,38} with projector augmented-wave (PAW) potentials.³⁹ We have treated Bi $5d^{10}6s^2$ and I $5s^25p^5$ as valence electrons. To ensure convergence with respect to the plane-wave

basis set, we used a cut-off energy of 450 eV. The exchange-correlation interactions were approximated using the Perdew, Burke and Ernzerhof (PBE) functional [40]. Ionic relaxations were carried out until the maximal Feynman-Hellman forces were less than 0.01 eV/Å. Because of the high relativistic effect of Bi element, we also included spin-orbit coupling (SOC). However, as SOC with the DFT-D3 functional severely underestimates the bandgap, we excluded SOC effects to calculate accurate vdW layer distance. We used the LOBSTER package to perform the COHP analysis [64,65]. Because spin-orbit coupling and COHP are incompatible, we performed the analysis with PBE and LDA functionals. More detailed information on the choice of SOC and vdW correction is discussed in Supplemental Materials [67].

Sample Preparation

The BiI₃ powder (99%, Aldrich) was used as a source without further purification for vapor phase deposition of BiI₃ thin films. A quartz tube mounted on a single zone furnace (Compact Split Tube Furnace with 1" Tube-OTF-1200X-S, MTI Corporation.) was used for all deposition studies. Silicon wafers (Test Grade, University Wafers Inc.) with or without a 100 nm thermal oxide layer, glass slides (48300-025, VWR) and pre-cut 5 mm x 5 mm high purity quartz substrates (MTI Corporation) were used as substrates for deposition.

The BiI₃ is kept in the middle of the quartz reactor where the temperature is 230 °C. BiI₃ has a melting point[66] of 402 °C but is known to sublime at a temperature of 237 °C [44]. Inert Ar gas was passed in the furnace at a flow rate of 280 standard cubic centimeters per minute (scm), and caused the transport of the sublimating BiI₃ vapor to the cooler zone in the downstream region. Condensation of the BiI₃ vapors takes place to produce the BiI₃ film consisting of

agglomerated, single crystalline hexagonally shaped microparticles as shown in Fig. 1a, at around 23 cm from the upstream side, where the temperature is maintained at 160 °C.

UV-VIS characterization

A UV–vis spectrophotometer (UV-1800, Shimadzu) was used to measure optical transmittance of the BiI₃ films on quartz substrates.

STEM characterization

Cross-sectional scanning transmission electron microscopy (STEM) analysis of BiI₃ thin films were performed using a probe aberration corrected microscope, a Jeol ARM 200cF STEM with a cold field emission source operated at 200 kV and equipped with a CEOS aberration corrector, at Universidad Complutense de Madrid, Spain. All STEM images shown in this work were acquired in the HAADF imaging mode, in which the contrast results from the high angle scattering strength. The intensity in the micrographs is approximately proportional to Z^2 , giving rise to so called Z-contrast imaging [46]. The STEM specimens were prepared using a FEI Dual Beam Helios Nanolab in the Advanced Microscopy Laboratory, Institute of Nanoscience of Aragon (INA- LMA).

The HAADF-STEM image simulations were performed by using the computem code [42,43]. The supercell structure model including the Bi bilayer was optimized using the DFT-D3 functional in DFT. The constructed supercell for the simulations consisted $9 \times 9 \times 30$ unit cells and the slice thickness was 1.0129 Å. The total thickness along the beam direction was 150 nm. Other parameters were set to the experimental imaging conditions.

AUTHOR INFORMATION

Corresponding Author

*Sung Beom Cho (cho.s@wustl.edu) and Rohan Mishra (rmishra@wustl.edu)

Present Addresses

[⊥]Department of Biomedical Engineering, Washington University, St. Louis, MO 63130, USA.

||Department of Nanotechnology and Advanced Materials, Sejong University, Seoul 05006, Republic of Korea.

Conflicts of interest

There are no conflicts on interest to declare

ACKNOWLEDGMENT

This work was supported by a start-up funding from Washington University and by a Ralph E. Powe Junior Faculty Enhancement Award from Oak Ridge Associated Universities to RM. This work used computational resources of the Extreme Science and Engineering Discovery Environment (XSEDE), which is supported by National Science Foundation grant number ACI-1053575. JG acknowledges Ramón y Cajal program (RyC-2012-11709). Authors acknowledge the ICTS-CNME for offering access to their instruments and expertise. The FIB microscopy work have been conducted in the "Laboratorio de Microscopias Avanzadas" at "Instituto de Nanociencia de Aragon - Universidad de Zaragoza.

References

- [1] Y. C. Kim, N. J. Jeon, J. H. Noh, W. S. Yang, J. Seo, J. S. Yun, A. Ho-Baillie, S. Huang, M. A. Green, and J. Seidal, *Adv. Energy Mater.* **6**, 1502104 (2016).
- [2] D. P. McMeekin, G. Sadoughi, W. Rehman, G. E. Eperon, M. Saliba, M. T. Hörantner, A. Haghighirad, N. Sakai, L. Korte, and B. Rech, *Science* **351**, 151 (2016).
- [3] D. W. deQuilettes, S. M. Vorpahl, S. D. Stranks, H. Nagaoka, G. E. Eperon, M. E. Ziffer, H. J. Snaith, and D. S. Ginger, *Science* **348**, 683 (2015).
- [4] H. Huang, M. I. Bodnarchuk, S. V. Kershaw, M. V. Kovalenko, and A. L. Rogach, *ACS Energy Lett.*, 2071 (2017).
- [5] W.-J. Yin, T. Shi, and Y. Yan, *Adv. Mater.* **26**, 4653 (2014).
- [6] W.-J. Yin, T. Shi, and Y. Yan, *Appl. Phys. Lett.* **104**, 063903 (2014).
- [7] A. Zakutayev, C. M. Caskey, A. N. Fioretti, D. S. Ginley, J. Vidal, V. Stevanovic, E. Tea, and S. Lany, *J Phys Chem Lett* **5**, 1117 (2014).
- [8] J. Kang and L.-W. Wang, *J. Phys. Chem. Lett.* **8**, 489 (2017).
- [9] A. Walsh and A. Zunger, *Nat Mater* **16**, 964 (2017).
- [10] R. E. Brandt, V. Stevanović, D. S. Ginley, and T. Buonassisi, *MRS Commun.* **5**, 265 (2015).
- [11] M.-H. Du and D. J. Singh, *Phys. Rev. B* **82**, 045203 (2010).
- [12] E. J. Juarez-Perez, R. S. Sanchez, L. Badia, G. Garcia-Belmonte, Y. S. Kang, I. Mora-Sero, and J. Bisquert, *J. Phys. Chem. Lett.* **5**, 2390 (2014).
- [13] W. J. Yin, T. Shi, and Y. Yan, *Adv Mater* **26**, 4653 (2014).
- [14] G. P. Nagabhushana, R. Shivaramaiah, and A. Navrotsky, *Proc. Natl. Acad. Sci.* **113**, 7717 (2016).
- [15] B. Conings, J. Drijkoningen, N. Gauquelin, A. Babayigit, J. D'Haen, L. D'Olieslaeger, A. Ethirajan, J. Verbeek, J. Manca, E. Mosconi, F. D. Angelis, H. and H.-G. Boyen, *Adv. Energy Mater.* **5**, 1500477, 1500477 (2015).
- [16] Y.-Y. Zhang, S. Chen, P. Xu, H. Xiang, X.-G. Gong, A. Walsh, and S.-H. Wei, *Chin. Phys. Lett.* **35** 036104 (2018).
- [17] A. S. Thind, X. Huang, J. Sun, and R. Mishra, *Chem. Mater.* **29**, 6003 (2017).
- [18] Z. Shi, J. Guo, Y. Chen, Q. Li, Y. Pan, H. Zhang, Y. Xia, and W. Huang, *Adv. Mater.* (2017).
- [19] A. M. Ganose, C. N. Savory, and D. O. Scanlon, *Chem. Commun.* **53**, 20 (2016).
- [20] X. Huang, S. Huang, P. Biswas, and R. Mishra, *J. Phys. Chem. C* **120**, 28924 (2016).
- [21] A. H. Slavney, T. Hu, A. M. Lindenberg, and H. I. Karunadasa, *J. Am. Chem. Soc.* **138**, 2138 (2016).
- [22] E. T. McClure, M. R. Ball, W. Windl, and P. M. Woodward, *Chem. Mater.* **28**, 1348 (2016).
- [23] M. R. Filip, S. Hillman, A. A. Haghighirad, H. J. Snaith, and F. Giustino, *J. Phys. Chem. Lett.* **7**, 2579 (2016).
- [24] R. E. Brandt, R. C. Kurchin, R. L. Hoye, J. R. Poindexter, M. W. Wilson, S. Sulekar, F. Lenahan, P. X. Yen, V. Stevanovic, J. C. Nino, M. G. Bawendi, and T. Buonassisi, *J. Phys. Chem. Lett.* **6**, 4297 (2015).
- [25] B. W. Park, B. Philippe, X. Zhang, H. Rensmo, G. Boschloo, and E. M. Johansson, *Adv. Mater.* **27**, 6806 (2015).

- [26] A. J. Lehner, D. H. Fabini, H. A. Evans, C.-A. Hébert, S. R. Smock, J. Hu, H. Wang, J. W. Zwanziger, M. L. Chabinye, and R. Seshadri, *Chem. Mater.* **27**, 7137 (2015).
- [27] A. J. Lehner, H. Wang, D. H. Fabini, C. D. Liman, C.-A. Hébert, E. E. Perry, M. Wang, G. C. Bazan, M. L. Chabinye, and R. Seshadri, *Appl. Phys. Lett.* **107**, 131109 (2015).
- [28] L. M. Wu, X. T. Wu, and L. Chen, *Coord. Chem. Rev.* **253**, 2787 (2009).
- [29] H. A. Evans, J. G. Labram, S. R. Smock, G. Wu, M. L. Chabinye, R. Seshadri, and F. Wudl, *Inorg. Chem.* **56**, 395 (2017).
- [30] N. J. Podraza, W. Qiu, B. B. Hinojosa, M. A. Motyka, S. R. Phillpot, J. E. Bacia, S. Trolier-McKinstry, and J. C. Nino, *J. Appl. Phys.* **114**, 033110 (2013).
- [31] A. C. Beer, R. K. Willardson, and E. R. Weber, *Semiconductors for Room Temperature Nuclear Detector Applications* (Elsevier Science, 1995).
- [32] P. J. Sellin, *Nucl Instrum Meth A* **513**, 332 (2003).
- [33] A. Owens and A. Peacock, *Nuclear Instruments and Methods in Physics Research Section A: Accelerators, Spectrometers, Detectors and Associated Equipment* **531**, 18 (2004).
- [34] A. T. Lintereur, W. Qiu, J. C. Nino, and J. Bacia, *Nucl. Instrum. Methods Phys. Res., Sect. A* **652**, 166 (2011).
- [35] L. Fornaro, A. Cuna, A. Noguera, M. Perez, and L. Mussio, *IEEE Trans. Nucl. Sci.* **51**, 2461 (2004).
- [36] M. Matsumoto, K. Hitomi, T. Shoji, and Y. Hiratate, *IEEE Trans. Nucl. Sci.* **49**, 2517 (2002).
- [37] R. E. Brandt, R. C. Kurchin, R. L. Hoye, J. R. Poindexter, M. W. Wilson, S. Sulekar, F. Lenahan, P. X. Yen, V. Stevanovic, J. C. Nino, M. G. Bawendi, and T. Buonasissi, *J Phys Chem Lett* **6**, 4297 (2015).
- [38] D. Nason and L. Keller, *Journal of Crystal Growth* **156**, 221 (1995).
- [39] J. P. Perdew, K. Burke, and M. Ernzerhof, *Phys. Rev. Lett.* **77**, 3865 (1996).
- [40] W.-B. Zhang, L.-J. Xiang, and H.-B. Li, *J. Mater. Chem. A* **4**, 19086 (2016).
- [41] A. Zakutayev, C. M. Caskey, A. N. Fioretti, D. S. Ginley, J. Vidal, V. Stevanovic, E. Tea, and S. Lany, *J. Phys. Chem. Lett.* **5**, 1117 (2014).
- [42] S. B. Zhang, S. H. Wei, A. Zunger, and H. Katayama-Yoshida, *Phys. Rev. B* **57**, 9642 (1998).
- [43] R. E. Brandt, J. R. Poindexter, P. Gorai, R. C. Kurchin, L. Nienhaus, M. W. B. Wilson, J. A. Polizzotti, R. Sereika, R. Žaltauskas, L. C. Lee, J. L. MacManus-Driscoll, M. Bawendi, V. Stevanović, and T. Buonasissi, *Chem. Mater.* **29**, 4667 (2017).
- [44] X. Chen, Y. Myung, A. Thind, Z. Gao, B. Yin, M. Shen, S. B. Cho, P. Cheng, B. Sadtler, R. Mishra, and P. Banerjee, *J. Mater. Chem. A* **5**, 24728 (2017).
- [45] S. J. Pennycook and D. E. Jesson, *Phys. Rev. Lett.* **64**, 938 (1990).
- [46] S. J. Pennycook and D. E. Jesson, *Ultramicroscopy* **37**, 14 (1991).
- [47] X.-H. Zhang, R.-W. Shao, L. Jin, J.-Y. Wang, K. Zheng, C.-L. Zhao, J.-C. Han, B. Chen, T. Sekiguchi, Z. Zhang, J. Zou, and B. Song, *Sci. Rep.* **5**, 10087 (2015).
- [48] T. Suzuki and M. Fujimoto, *J. Appl. Phys.* **89**, 5622 (2001).
- [49] S. Grimme, J. Antony, S. Ehrlich, and H. Krieg, *J. Chem. Phys.* **132**, 154104 (2010).
- [50] S. Grimme, S. Ehrlich, and L. Goerigk, *J. Comput. Chem.* **32**, 1456 (2011).
- [51] G. Jezequel, J. Thomas, and I. Pollini, *Phys. Rev. B* **56**, 6620 (1997).
- [52] F. Dong, T. Xiong, Y. Sun, Z. Zhao, Y. Zhou, X. Feng, and Z. Wu, *Chem. Commun.* **50**, 10386 (2014).
- [53] K. Catchpole and A. Polman, *Opt. Express* **16**, 21793 (2008).

- [54] H. A. Atwater and A. Polman, *Nat. Mater.* **9**, 205 (2010).
- [55] J. D. Major, *Semicond. Sci. Technol.* **31**, 093001 (2016).
- [56] B. Yang, O. Dyck, J. Poplawsky, J. Keum, A. Poretzky, S. Das, I. Ivanov, C. Rouleau, G. Duscher, D. Geohegan, and K. Xiao, *J. Am. Chem. Soc.* **137**, 9210 (2015).
- [57] H. Li, X. X. Liu, Y. S. Lin, B. Yang, and Z. M. Du, *Phys. Chem. Chem. Phys.* **17**, 11150 (2015).
- [58] U. H. Hamdeh, R. D. Nelson, B. J. Ryan, U. Bhattacharjee, J. W. Petrich, and M. G. Panthani, *Chem. Mater.* **28**, 6567 (2016).
- [59] P. A. Sant and P. V. Kamat, *Phys. Chem. Chem. Phys.* **4**, 198 (2002).
- [60] J. A. Hachtel, R. Sachan, R. Mishra, and S. T. Pantelides, *Appl. Phys. Lett.* **107**, 091908 (2015).
- [61] A. Llordes, G. Garcia, J. Gazquez, and D. J. Milliron, *Nature* **500**, 323 (2013).
- [62] W. J. Kaiser, E. M. Logothetis, and L. E. Wenger, *Solid State Commun* **58**, 83 (1986).
- [63] J. C. M. Garnett, *Philos. Trans. R. Soc Lond.* **203**, 385 (1904).
- [64] R. Dronskowski and P. E. Bloechl, *J. Phys. Chem.* **97**, 8617 (1993).
- [65] S. Maintz, M. Esser, and R. Dronskowski, *Acta Phys. Pol. B* **47** (2016).
- [66] A. Cuña, I. Aguiar, A. Gancharov, M. Pérez, and L. Fornaro, *Cryst. Res. Technol.* **39**, 899 (2004).
- [67] See Supplemental Material at [URL] for 1. Discussion on exchange-correlation functional 2. Details of point defects modeling, 3. Calculation details on carrier concentration calculation 4. Absorption spectra calculation 5. XRD diffraction 6. Atomic configuration of point defects 7. Defect calculation with PBE-optimized lattice constant 8. The STEM intensity profile on point defects 9. Defect formation energy under intermediate condition 9. Tested atomic configuration of intergrowth candidates 10. Structure of Bi semimetal

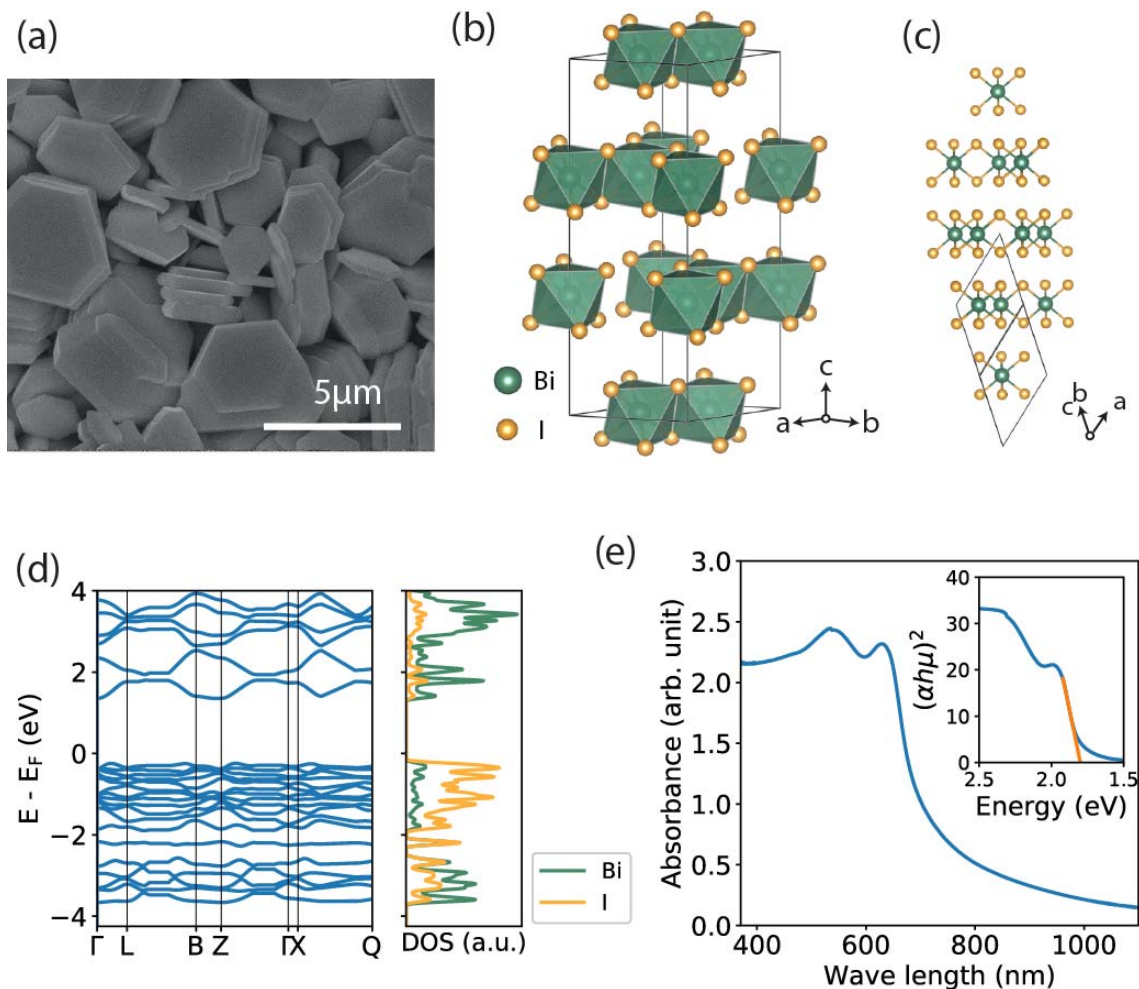


Figure 1 (a) SEM image of the synthesized BiI₃ thin-film. (b) Atomic structure of BiI₃ crystal in conventional unit cell. It consists of I-Bi-I trilayer. $2/3^{\text{rd}}$ of the octahedral sites are occupied by Bi while $1/3^{\text{rd}}$ are vacant. (c) Primitive unit cell of BiI₃ crystal with $(2 \times 2 \times 2)$ periodicity. It shows an *ABCABC* stacking pattern. (d) Calculated band structure and density of states (DOS) of primitive cell of BiI₃. (e) UV-vis spectra of the synthesized thin film.

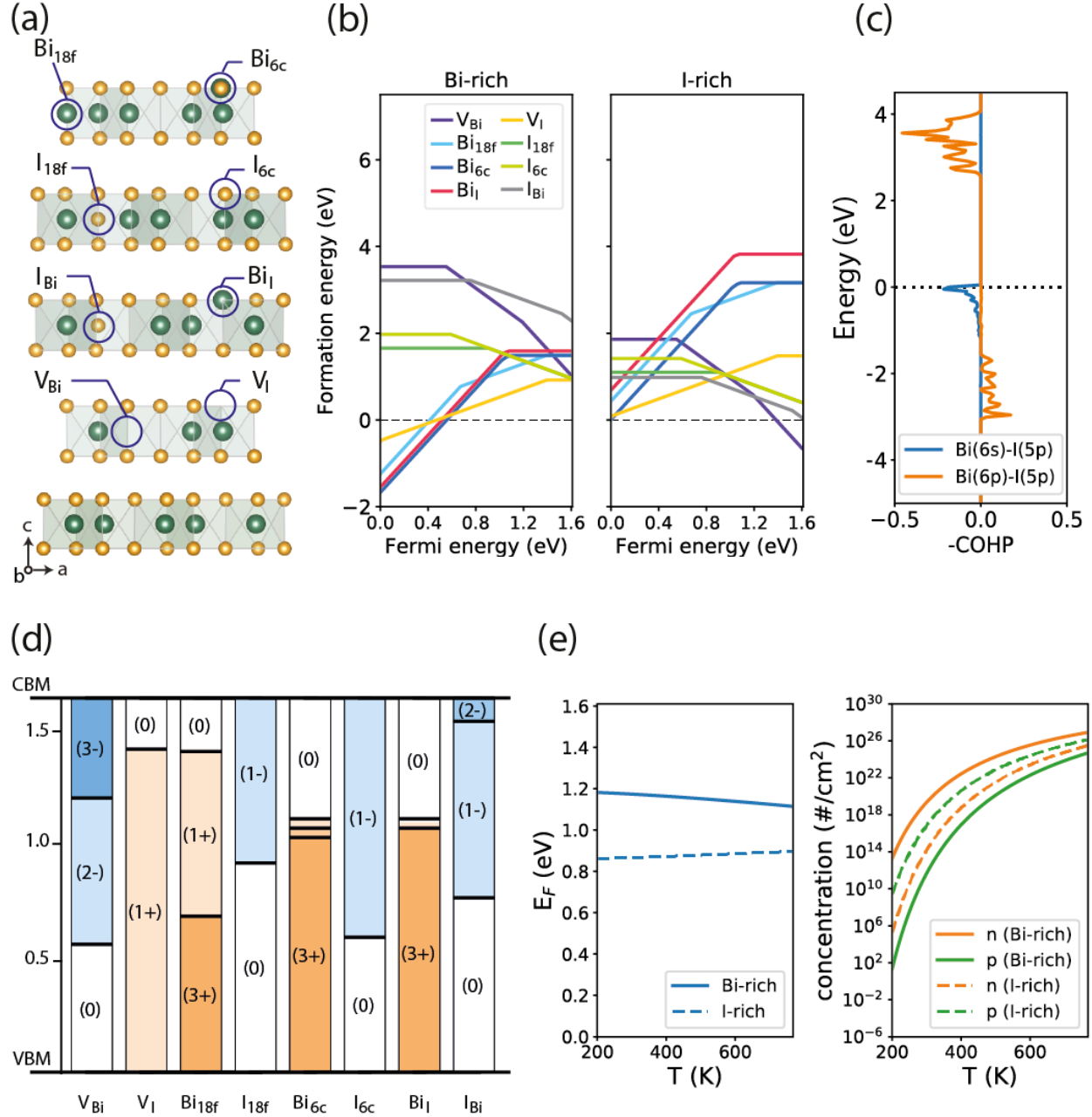


Figure 2 (a) Atomic configuration of all possible native point defects in BiI₃. (b) Calculated formation energy of point defects under Bi-rich and I-rich preparation conditions obtained using PBE functional with spin-orbit coupling with experimental lattice constants. (c) Crystal Orbital Hamiltonian Population (COHP) analysis of BiI₃. The energy is referenced to the valence band maximum. Both the valence band and conduction band are dominated by antibonding states. (d) Equilibrium charge state and thermodynamic transition level for the various point defects as a function of Fermi level. All the defects show transition level from neutral state to a charged state ‘deep’ within the band gap, which shows that BiI₃ is not a defect-tolerant material. (e) Fermi level and carrier concentration calculated from the formation energy of the point defects. The Fermi level is almost pinned under both the preparation conditions due to the presence of deep-level defects. The Bi-rich condition is expected to generate more carriers than I-rich condition.

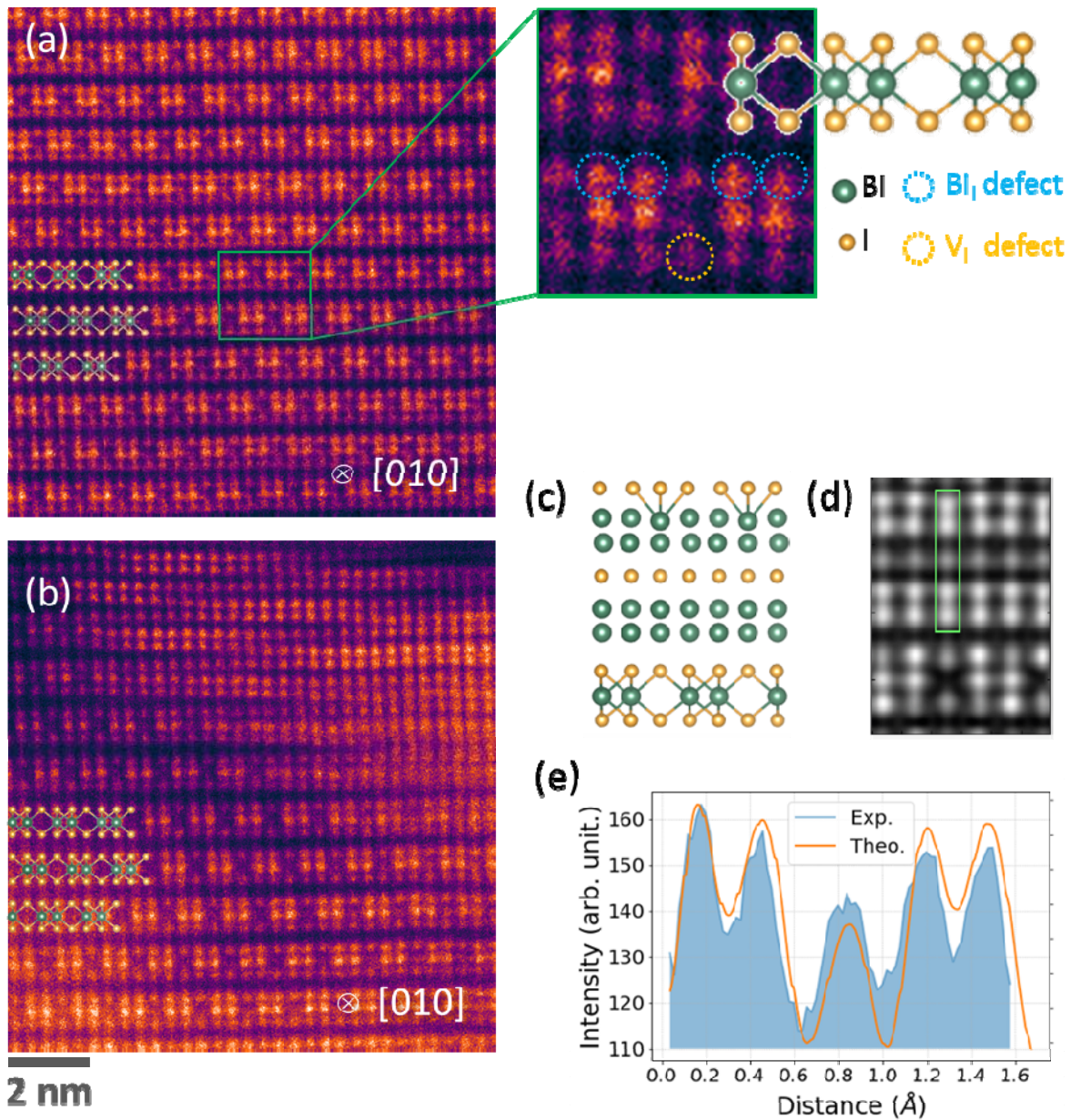


Figure 3 (a) HAADF-STEM image of the BiI_3 structure from a defect-free region of the film viewed along the $[010]$ zone axis. It shows the I-Bi-I layered structure of BiI_3 with its $2/3^{\text{rd}}$ occupancy of the Bi sublattice. From the overlapping images, $1/3^{\text{rd}}$ missing occupancy of Bi within the layers shows ABCABC stacking. Inset shows a magnified image of the BiI_3 matrix along with the atomic structure of a layer of BiI_3 . Bi_I and V_I defects are marked in blue and yellow, respectively. (b) HAADF-STEM image of a BiI_3 thin-film region showing the presence of several Bi intergrowths. (c) The constructed atomic structure of the Bi intergrowths. (d) Simulated STEM image of the defective structure shown in (c). (e) Intensity profiles of both the simulated and experimental STEM images along a square region like the one marked in (d).

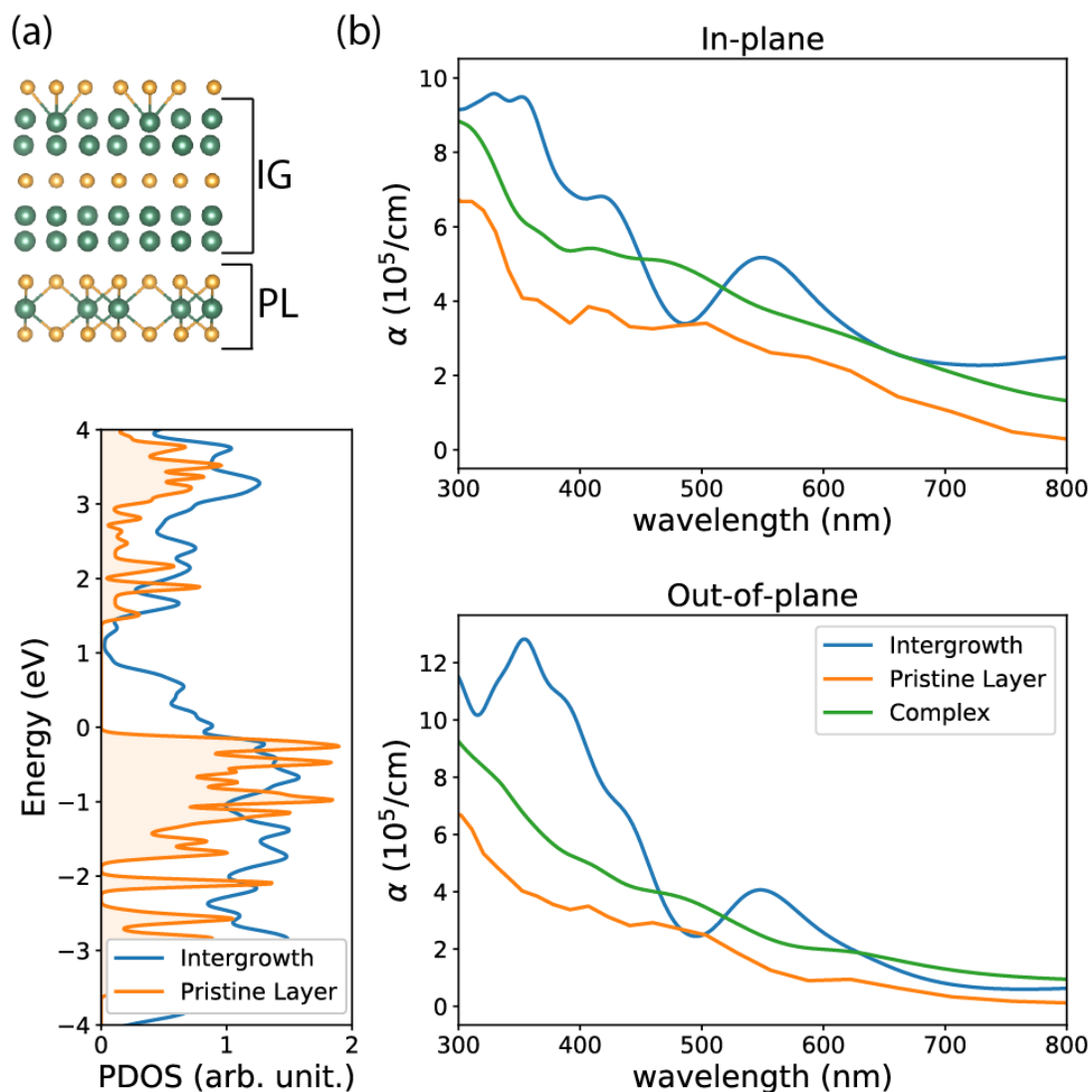


Figure 4 (a) Projected density of states (PDOS) of the Bi intergrowth layer (IG) and a pristine layer (PL) of BiI₃. The pristine BiI₃ to intergrowth layer ratio in the calculated cell is 1:2. The stacking fault shows metallic nature. (b) Absorption spectra of the pure intergrowth, pristine BiI₃, and the composite cell with a layer ratio of 2:1. The composite shows increase in absorbance over the individual units for a large frequency range.